

The Impact of Thermal Variations of HST on Background Light Estimates

by

Isabel McIntyre

A Dissertation Presented in Partial Fulfillment
of the Requirements for the Degree
Master of Science

Approved October 2024 by the
Graduate Supervisory Committee:

Dr. Rogier Windhorst, Chair
Dr. Timothy Carleton
Dr. Rolf Jansen

ARIZONA STATE UNIVERSITY

December 2024

©2024 Isabel McIntyre
All Rights Reserved

ABSTRACT

The SKYSURF project constrained extragalactic background light (EBL) and diffuse light with the vast archive of Hubble Space Telescope (HST) images. Thermal emission from HST itself introduces an additional uncertain background and hinders accurate measurement of the diffuse light level. Here, I use archival WFC3/IR engineering data to investigate and model changes in the temperature of various components in HST's optical path as a function of time (solar cycle) and time of the year (Earth-Sun distance). I also specifically investigate changes in temperature with HST's orbital phase and time since Earth occultation. I investigate possible correlations between HST component temperature and year, and temperature and month. The thermal background changes by less than one Kelvin in the WFC3 pick-off mirror, one of the most important contributors to the thermal background. I model these data to describe the impact that orbital phase, year, and time of year have on the HST and WFC3 component temperatures, and use this to derive the impact on the thermal dark signal and the resulting diffuse light measurements. Based on this improved modeling, I provide new upper limits on the level of diffuse light of $21 \text{ nW m}^{-2} \text{ sr}^{-1}$, $32 \text{ nW m}^{-2} \text{ sr}^{-1}$, and $25 \text{ nW m}^{-2} \text{ sr}^{-1}$ for F125W, F140W, and F160W. Additionally, by accounting for all known sources of measurement uncertainty, I report lower limits on the level of diffuse light of $12 \text{ nW m}^{-2} \text{ sr}^{-1}$, $20 \text{ nW m}^{-2} \text{ sr}^{-1}$, and $2 \text{ nW m}^{-2} \text{ sr}^{-1}$ for F125W, F140W, and F160W.

ACKNOWLEDGMENTS

I would like to thank all those who have supported me and taught me while I have been at ASU. In particular, I would like to thank my advisors Dr. Rogier Windhorst, Dr. Timothy Carleton, and Dr. Elizabeth Trembath-Reichert. Thank you for all that you have taught me and all you continue to teach me, and for making my time at ASU so wonderful.

I would also like to thank the other members of my committee and of my research group who have helped guide me, Dr. Rolf Jansen and Dr. Seth Cohen. Furthermore, I'd like to thank Rosalia O'Brien, Darby Kramer, and Alex Pigarelli for your companionship and for all of the help you've given me over the years. I'd also like to thank the other co-authors of my recent paper regarding this work, Sarah Caddy, Dr. John MacKenty, Dr. Scott Kenyon, and Dr. Richard Arendt. The advice and help everyone here has given me has been invaluable.

I would like to thank all of my friends and family who have stood by me while I have been a graduate student. In particular, I would like to thank Kaylee Neat, Jaya Nagarajan-Swenson, and Lindsey Hands for their unwavering support since our time as undergraduates together. I would not be where I am without you.

I would also like to give my deepest gratitude to my parents MaryAnn and Michael, to my sisters Bridget, Clare, and Ellen, and to my grandparents William B., Ljubica, William M., and Mary for constantly encouraging me to follow my interests and do what I love, for always listening to me talk about what I do, and for everything else you've done for me. I love you all very much.

Finally, I would like to acknowledge the twenty two Native Nations that have inhabited this land for centuries. Arizona State University's four campuses are located in the Salt River Valley on ancestral territories of Indigenous peoples, including the

Akimel O'odham (Pima) and Pee Posh (Maricopa) Indian Communities, whose care and keeping of these lands allows us to be here today. We acknowledge the sovereignty of these nations and seek to foster an environment of success and possibility for Native American students and patrons.

TABLE OF CONTENTS

	Page
LIST OF TABLES	vi
LIST OF FIGURES	vii
CHAPTER	
1 INTRODUCTION	1
2 HST TEMPERATURE DATA	5
3 SHORT-TERM TEMPERATURE CHANGES	7
4 LONG-TERM TEMPERATURE CHANGES	11
5 DISCUSSION	17
6 CONCLUSION AND FUTURE OUTLOOK	23
NOTES	23
.....	25
BIBLIOGRAPHY	25
APPENDIX	

LIST OF TABLES

Table	Page
1. The default temperature (T_{ref}) and thermal signal from HST's optical components.	6
2. Thermal dark corrections (in e-/pix/s) for all of the WFC3/IR filters included in this study.	17
3. The diffuse light measurements of Carleton <i>et al.</i> (2022), O'Brien <i>et al.</i> (2023), and this work based on the combined primary, secondary, and T_{POM} temperatures. Conversions between MJy/sr to $\text{nW m}^{-2} \text{sr}^{-1}$ were done using the multipliers in Carleton <i>et al.</i> (2022).	18

LIST OF FIGURES

Figure	Page
<p>1. Schematic of HST Wide Field Camera 3 (WFC3), adapted from MacKenty <i>et al.</i> (2010). The components of the WFC3 that we focus on for this paper are the pick-off arm, which holds the pick-off mirror, and components near the infrared cold enclosure and filters.</p>	2
<p>2. Time since occultation (seconds) versus average T_{POM} (in degrees Celsius) with orbital phase in 45 degree bins. For any time value greater than 6000 seconds, a value of 6000s is assigned. Data was obtained for each month of January only for the years 2015 through 2023. Errors are calculated as the standard deviation of the residuals in Figure 7.</p>	8
<p>3. Orbital phase (degrees) versus average T_{POM} (degrees Celsius). The orbital phase is binned over 50 degrees, and data are grouped by time since occultation in 1000s bins. Data was obtained for each month of January for 2015 through 2023. Errors are calculated as the standard deviation of the residuals in Figure 7.</p>	8
<p>4. Pick-off arm temperature as a function of day of the year. Top: Pick-off arm temperature vs. orbital phase (degrees) and day of the year. Bottom: Pick-off arm temperature vs. time since occultation (seconds) and the day of the year. The color represents T_{POM} ($^{\circ}\text{C}$).</p>	9
<p>5. Pick-off arm temperature vs. day of the year and orbital phase (degrees), where the color represents T_{POM} (degrees Celsius). The horizontal red lines indicate where the Earth is closest to the Sun and the horizontal blue lines indicate where Earth is furthest from the Sun.</p>	12

Figure	Page
6. Optical bench temperature vs. day of the year and orbital phase (degrees), where the color representing average optical bench temperature (degrees Celsius).....	13
7. Model of the deviation in T_{POM} from the average yearly temperature as a function of the Earth-Sun distance. Error bars are calculated as the standard deviation of the residual.....	14
8. Temperatures of other WFC3 hardware components. Top: Temperature change of the IR focal plane array using data from 2009 through 2022. Middle: Temperature change of the optical bench condenser saddle using data from 2009 through 2022. Bottom: Temperature change of the optical bench cold plate using data from 2009 through 2022.	15
9. Top: Sky surface brightness measurements from this work for maximum and minimum (T_{POM}) and M1 temperature measurements, compared to those from Bernstein <i>et al.</i> (2002), Matsuura <i>et al.</i> (2017), and O'Brien <i>et al.</i> (2023), and the zodiacal light models from Aldering (2001) and Kelsall <i>et al.</i> (1998). The vertical line in the top left of the plot represents the average size of the error bars for these measurements. Errors are assumed to be approximately 3%, per Windhorst <i>et al.</i> (2022). Bottom: A zoomed-in version of the top plot to highlight the differences between instrument components and maximums and minimums.	19

Figure	Page
10. The diffuse light measurements found in Dube <i>et al.</i> (1979), Dwek and Arendt (1999), Cambr�esy <i>et al.</i> (2001), Bernstein <i>et al.</i> (2002), Arendt and Dwek (2003), Levenson <i>et al.</i> (2007), Mattila <i>et al.</i> (2017), Matsuura <i>et al.</i> (2017), Sano <i>et al.</i> (2020), Lauer <i>et al.</i> (2022), Symons <i>et al.</i> (2023), and Postman <i>et al.</i> (2024) compared with our upper and lower limits on diffuse light. Our limits are lower than the previous measurements of diffuse light. .	20
11. Top left: Residual between O’Brien <i>et al.</i> (2023) sky surface brightness measurements and Kelsall <i>et al.</i> (1998) zodiacal light model (extrapolated to redder wavelengths following Carleton <i>et al.</i> (2022)) in the F125W filter using the thermal dark correction from Carleton <i>et al.</i> (2022). The red line is the line of best fit for these data. Top right: Residual between O’Brien <i>et al.</i> (2023) sky surface brightness measurements and Kelsall <i>et al.</i> (1998) zodiacal light model in the F125W filter using the empirical thermal dark correction this work. The red line is the line of best fit for these data. Middle left: Same as top left, but using the F140W filter. Middle right: Same as top right, but using the F140W filter. Bottom left: Same as top left, but using the F160W filter. Bottom right: Same as top right, but using the F160W filter.	21

Chapter 1

INTRODUCTION

Project SKYSURF (Windhorst *et al.*, 2022) uses Hubble Space Telescope (HST) archival images to measure the sky surface brightness between all detected discrete objects and constrain measurements of diffuse light (DL; Carleton *et al.* 2022; O’Brien *et al.* 2023). The near-infrared extragalactic background light (EBL) is an important descriptor of the Universe because it reflects the total incident flux of all objects, both identified and undetected, in the Universe (McVittie and Wyatt, 1959; Partridge and Peebles, 1967; Matsumoto *et al.*, 2005; Kneiske and Dole, 2010; Cooray, 2016). An accurate EBL measurement can be used to better understand galaxy assembly over cosmic time. If all galaxies are accounted for, then direct measurements of the EBL level should match the measurements predicted by integrated galaxy counts (Cooray 2016; Driver *et al.* 2016; Koushan *et al.* 2021; Windhorst *et al.* 2023). If direct EBL measurements exceed the integrated galaxy light (IGL), it could indicate the presence of light from undetected sources, such as low surface brightness galaxies, intra-halo light (Conselice *et al.*, 2016; Lauer *et al.*, 2021), or light from early galaxy formation and reionization (Santos *et al.*, 2002; Cooray *et al.*, 2004; Kashlinsky *et al.*, 2004).

One possible contributor to systematic errors in the measurements of DL is the thermal emission from the instruments used to detect it (Carleton *et al.*, 2022). In particular, the Wide Field Camera 3 (WFC3) imager on the Hubble Space Telescope HST, with ultraviolet and near-infrared capabilities (Dressel and Marinelli, 2023, Figure 1), was used for diffuse light constraints in Carleton *et al.* (2022). WFC3 was installed as part of HST Servicing Mission 4 in May 2009 and began operations in June 2009 (Dressel and Marinelli, 2023). The WFC3/IR channel observes at wavelengths of 800 nm to 1700 nm (Dressel and Marinelli, 2023). As such, it is important for the instrument’s temperature to remain cool and stable to minimize the contamination of its resulting images by thermal emission from the WFC3 camera hardware itself. The ideal temperature for WFC3 operation is 145 K, and a set of thermoelectric coolers (TECs) are used to cool the instrument, as described in Dressel and Marinelli (2023) and also in Appendix A of Carleton *et al.* (2022).

The optical bench is the component of the instrument which houses the instrument’s optics. This hardware is most likely to impact the WFC3/IR observations, and therefore should have the coolest and most stable temperatures. Several temperature sensors are located near the optical bench, including near the IR fold mirror, M1 mirror mount, top cover, cold plate, and condenser saddle. The IR fold mirror directs incoming light into the IR channel of WFC3 (Sahu, 2021), and has an average temperature of 3.90 °C. The mount for the M1 mirror, which also helps to reimage the

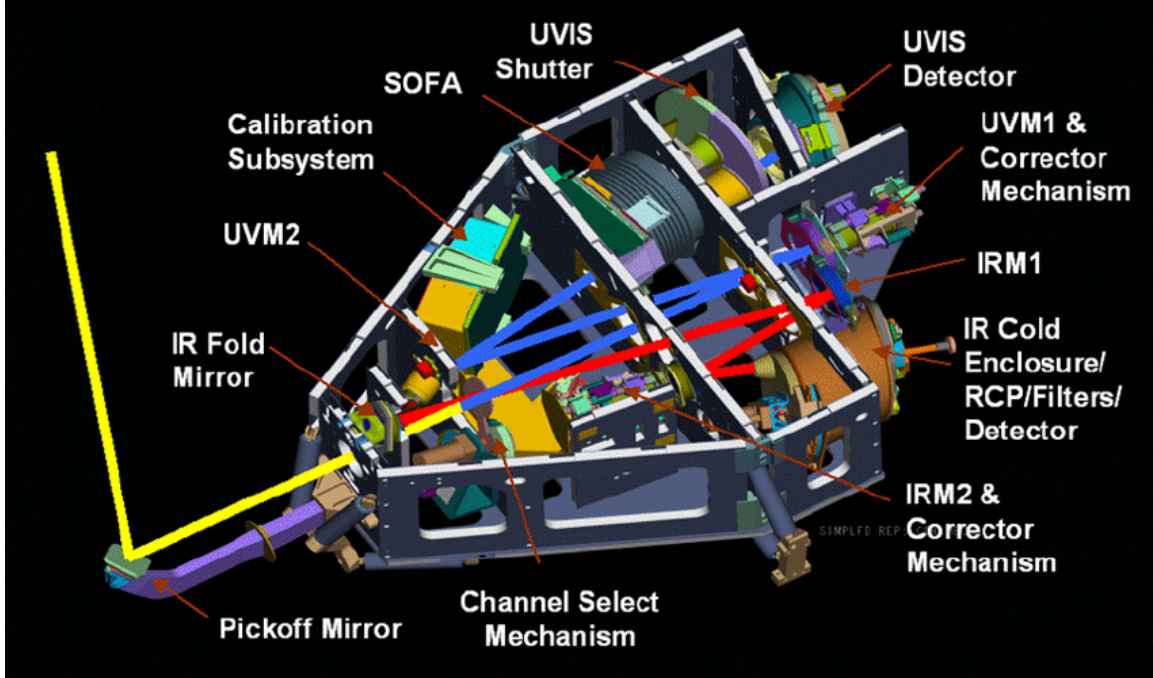


Figure 1 Schematic of HST Wide Field Camera 3 (WFC3), adapted from MacKenty *et al.* (2010). The components of the WFC3 that we focus on for this paper are the pick-off arm, which holds the pick-off mirror, and components near the infrared cold enclosure and filters.

light (MacKenty *et al.*, 2010), has an average temperature of -4.45°C . The cold plate helps to cool the IR optics and is nominally operated at $-5 \pm 2^{\circ}\text{C}$ (Cleveland *et al.*, 2003), and based on HST data operates at an average temperature of 3.90°C . The sensor near the condenser saddle, which is a component of the heat pipe that helps maintain WFC3's temperature (Cleveland *et al.*, 2003), has an average temperature of -38°C . There is also a notable temperature sensor on the pick-off arm, which holds the instrument's pick-off mirror and has an average temperature of 12.32°C . Because of its distance from the cooling components near the optical bench, this component was expected to have the most variability in its temperature.

Despite the importance of maintaining cool temperatures within WFC3, no studies have been conducted in the last 15 years since its launch regarding how well the instrument cools. While temperature changes in WFC3 have not been studied, studies have been conducted regarding changes in the temperature of the Near Infrared Camera and Multi-Object Spectrometer (NICMOS) (Sosey and Sivaramakrishnan, 2004). An increase in temperature by 17.1K was noted in the detector, which was expected, and the authors note that the installation of additional instruments contributed to the increase in temperature (Sosey and Sivaramakrishnan, 2004).

In this paper, we investigate the impact of thermal emission from WFC3 itself

on measurements of DL levels. In Carleton *et al.* (2022), an initial estimate the temperature of, and therefore the thermal dark emission from WFC3, used to constrain the DL levels. However, uncertainties in the true temperature of HST, as well as any possible temporal variation in the temperature of HST can cause estimates of the DL levels may be overestimated in some observations and underestimated in others. By investigating how WFC3's temperature changes with orbital phase, time since Earth-occultation (which is defined as when HST was looking at the Earth), year, and day of the year, we can more accurately account for changes in *HST*'s temperature. In Chapter 2, we discuss the WFC3/IR data collected for this project. In Chapters 3 and 4, we discuss how we utilized this data to identify potential trends in WFC3's temperature as a function of time and share the trends that we have identified. In Chapter 5 we discuss the implications of these findings for the levels of diffuse light that may be present.

Chapter 2

HST TEMPERATURE DATA

To conduct this analysis, we accessed all publicly available archival WFC3 data from the Barbara A. Mikulski Archive for Space Telescopes (MAST) from June 2009 through December 2022. Specifically, we obtained all “spt”, “jit”, and “ima” fits files associated with WFC3/IR exposures. To obtain these data, we filtered for all data types and selected only the WFC3 instrument. We also added the column “aperture” and set the condition to “IR”. Then, we filtered by date to select all data between June 2009 and December 2022. We chose to specifically focus on WFC3/IR exposures because the effect of thermal noise on shorter wavelengths is minimal (O’Brien *et al.*, 2023). From the “spt” files, we obtained temperature data for the infrared focal plane array, optical bench near the IR fold mirror, infrared fold mirror, optical bench near the IR M1 mount, optical bench on the top cover, optical bench cold plate, detector radiator on the IR side by the condenser, detector radiator on IR side away from saddle, optical bench cold plate condenser saddle, and IR detector baseplate evaporator saddle. Particular attention was paid to the pick-off arm temperature (T_{POM}) due to its increased sensitivity to changes in temperature and to sensors near the optical bench, because of its proximity to the filter wheel, where most of the thermal effect is expected to come from. Table 1 shows the default temperature values (referred to as T_{ref} throughout this work) of the HST optical components and the thermal background they contribute. Table 1 shows the default temperature values (referred to as T_{ref} throughout this work, and taken from published reference tables¹

The “spt” file notes the RA of the Sun during the observation. The “ima” file was used to obtain the date of the observation and the readout time. The readout time was used along with HST’s longitude during the course of the observation to calculate the difference in RA between HST and the Sun. This difference indicates the position of HST in its orbit, referred to as ΔRA , following Sunnquist *et al.* (2017).

Information from the “spt” and “jit” files were used to calculate time since Earth occultation. One potential cause of thermal variations is if HST has recently pointed at Earth. To test this, we consider the time since HST was pointed at the Earth. To calculate this, we extrapolated HST’s position over the previous orbit and found the time for which the angle between HST’s target and the Earth was less than the apparent angular size of the Earth (67°) seen from Low Earth Orbit (LEO).

¹<https://hst-crds.stsci.edu/>) of the HST optical components and the thermal background they contribute, as determined from the Carleton *et al.* (2022) thermal model.

Component	Temperature (°C)	Thermal Background (e-/s/pix) in F160W
Primary Mirror	15.15	0.016
Mirror Pads	15.15	0.007
Secondary Mirror	17.15	0.027
Pick-off Mirror	14.75	0.026
IR Chanel Select Mechanism	0.15	0.002
Fold Mirror	0.15	0.002
WFC3IR Mirror 1	0.15	0.002
WFC3IR Mirror 2	0.15	0.002
WFC3IR Refractive Corrector Plate	-35.85	<0.001
WFC3IR Filter	-35.85	0.003
Total		0.087

Table 1 The default temperature (T_{ref}) and thermal signal from HST's optical components.

Some sensors were limited in their sensitivity to changes in temperature. For instance, the sensor near the pick-off mirror arm only read two temperatures: 12.8571 and 12.1429 °C. To account for this, the temperature of each sensor was averaged over 50 day bins. Furthermore, we use temperatures of all components reported in "spt" files to account for the range of temperatures across the instrument.

Chapter 3

SHORT-TERM TEMPERATURE CHANGES

We investigated temperature as a function of time since occultation and orbital phase given the possible influence of: (a) incoming radiation from pointing the telescope at Earth, and (b) radiation from HST being on the day-side of the Earth. Figure 2 shows the relation between time since Earth occultation and T_{POM} . To evaluate the level of correlation between time since occultation at varying orbital phases and temperature, we calculated the Pearson correlation coefficients of these data.

Figure 3 shows how T_{POM} is impacted by orbital phase. T_{POM} changes with orbital phase by less than 1 °C. Temperature increases where orbital phase goes from 0 to 100 degrees, decreases from 100 to 250 degrees, then increases again. Overall, we find that T_{POM} is stable over the course of its orbit and is therefore not affected by earthshine. At orbital phases smaller than 270°, a negative correlation was observed, with correlation coefficients ranging from -0.96 to -0.10 . At orbital phases larger than 270°, the correlation coefficients are positive. From 270 to 315°, the correlation coefficient is -0.89 , and from 315 to 360°, the correlation coefficient is 0.65 . However, the p-values for all ranges of significance are greater than 0.05, with the exception of the 45–90° group, whose correlation coefficient has a p-value of 0.04. Therefore, we cannot consider these correlations to be significant. While there is no clear trend with time since occultation, there is a distinction between T_{POM} at different orbital phases.

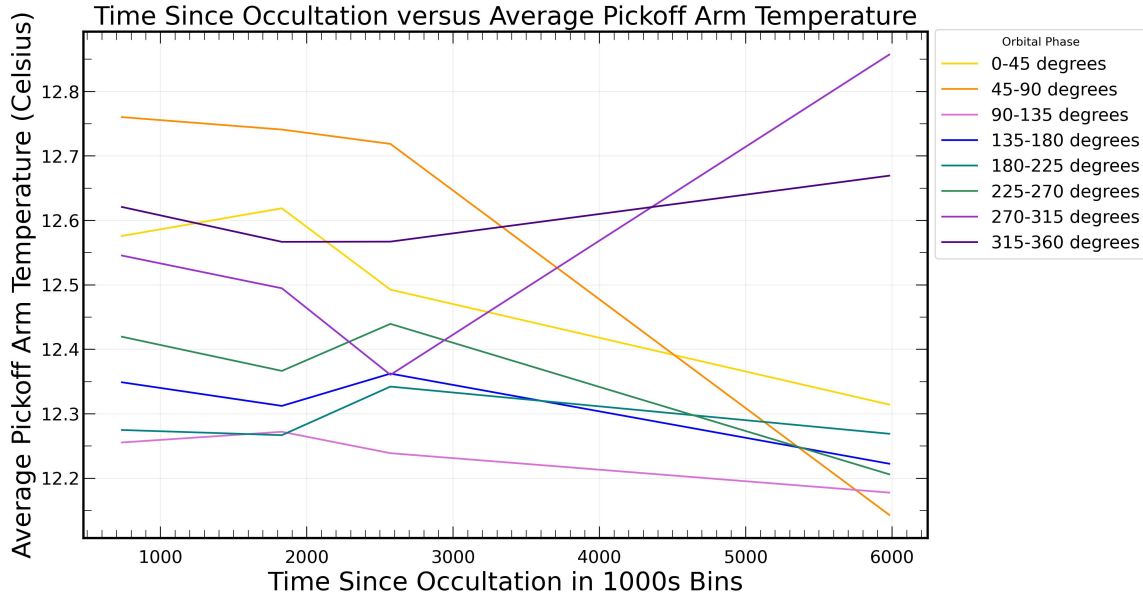


Figure 2 Time since occultation (seconds) versus average T_{POM} (in degrees Celsius) with orbital phase in 45 degree bins. For any time value greater than 6000 seconds, a value of 6000s is assigned. Data was obtained for each month of January only for the years 2015 through 2023. Errors are calculated as the standard deviation of the residuals in Figure 7.

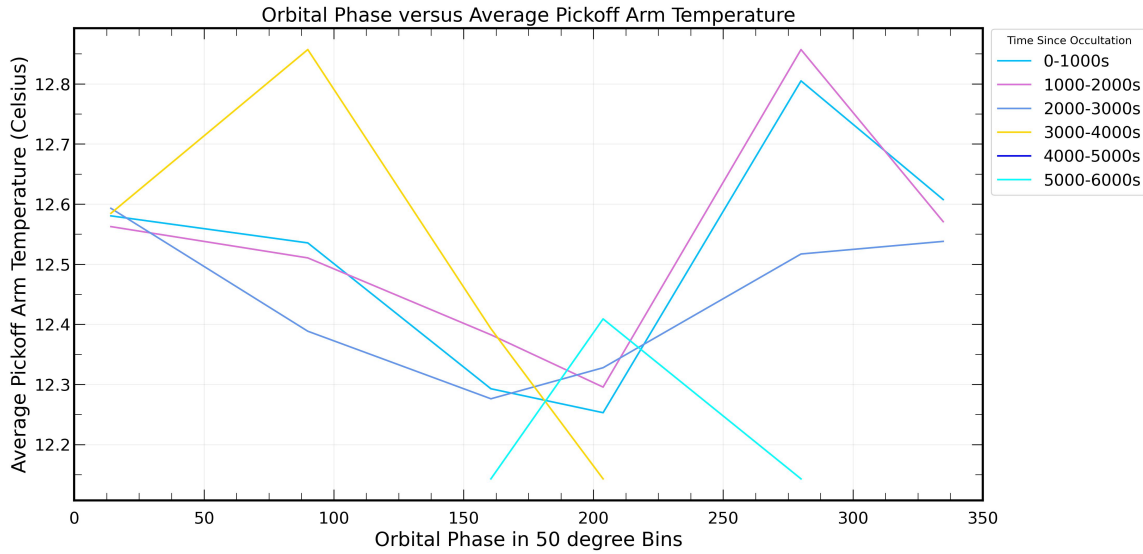


Figure 3 Orbital phase (degrees) versus average T_{POM} (degrees Celsius). The orbital phase is binned over 50 degrees, and data are grouped by time since occultation in 1000s bins. Data was obtained for each month of January for 2015 through 2023. Errors are calculated as the standard deviation of the residuals in Figure 7.

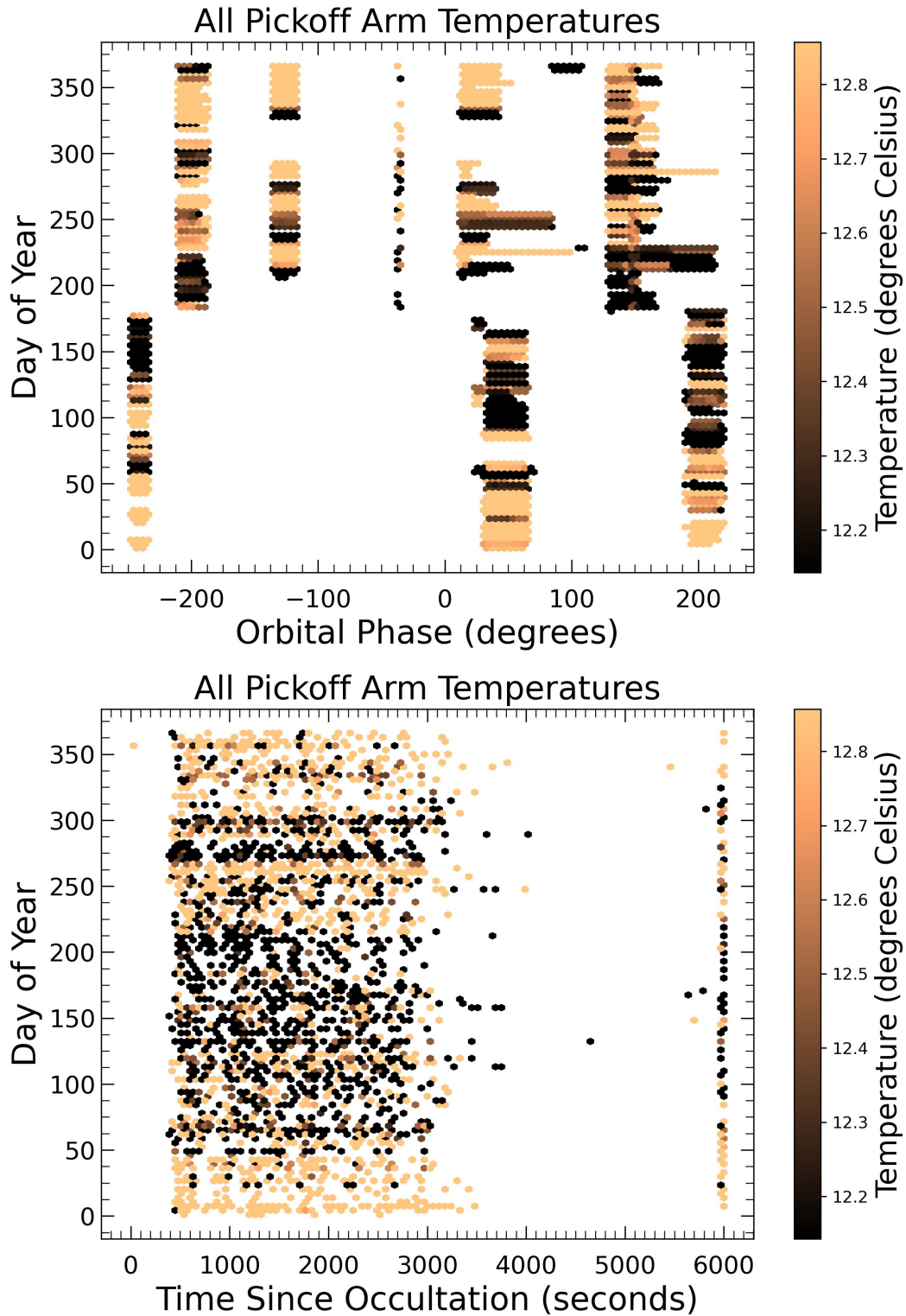


Figure 4 Pick-off arm temperature as a function of day of the year. **Top:** Pick-off arm temperature vs. orbital phase (degrees) and day of the year. **Bottom:** Pick-off arm temperature vs. time since occultation (seconds) and the day of the year. The color represents T_{POM} ($^{\circ}\text{C}$).

Chapter 4

LONG-TERM TEMPERATURE CHANGES

Although we identify some short-term T_{POM} changes identified, we find that T_{POM} is more significantly impacted by the Earth’s orbit around the Sun and yearly variations, rather than the LEO orbital phase or time since Earth occultation. Figure 4a shows the average T_{POM} as a function of day of the year and orbital phase. The temperature is coolest during the middle of the calendar year (July–August), when the Earth is furthest from the Sun, as and warmest during the beginning and end of the year (December–January), when the Earth is closest to the Sun. However, consistent with the results of Chapter 3, there is no noticeable trend in temperature with orbital phase at a given time of the year. Similarly, Figure 4b shows T_{POM} as a function of time since occultation and day of the year. This result shows the same trend with increased temperatures earlier and later in the calendar year, and decreased temperature in the middle of the calendar year, with little or no dependence on time since occultation evident.

We identify the observed variation in T_{POM} over the course of a year since WFC3 began operation in 2009 (Figure 5). While some years exhibit less thermal variation than others, in all years temperatures tend to be cooler when Earth is furthest from the Sun (as shown by the blue line in Figure 5, and warmer when Earth is closest to the Sun (as depicted by the red line) In Figure 6, we observe the same trend across another component of the instrument.

To investigate this further, we examined the relationship between T_{POM} and Earth-Sun distance. Figure 7 shows decreasing temperature with increasing Earth-Sun distance. Here, we focus specifically on the deviation of the temperature from the yearly average to account for variations in the instrument’s temperature from year to year. We use a linear regression to fit the data points and find that

$$\Delta(T_{\text{POM}}) = -4.22d + 4.21, \quad (4.1)$$

where $\Delta(T_{\text{POM}})$ refers to the deviation in T_{POM} from the yearly average in Kelvin and d refers to the Earth-Sun distance in AU. This model has an r-value of -0.75, which is calculated using a Pearson correlation coefficient (Virtanen *et al.*, 2020), and a high degree of confidence with a p-value of 0.0005.

We also found that average T_{POM} changes from year to year in Figure 5. The temperature was initially high in 2009 at the start of WFC3 operations, and cooled from 2009 until the mid-2010s. However, by 2017 and through the present day, T_{POM} has been increasing again. While it is unclear what causes these yearly variations, one possibility is that the cooling equipment onboard *HST* was able to cool the instrument down to a certain point, before the slow degradation of the multi-layer insulation (MLI) on *HST*’s outer tube caused T_{POM} to increase again. Another possible explanation

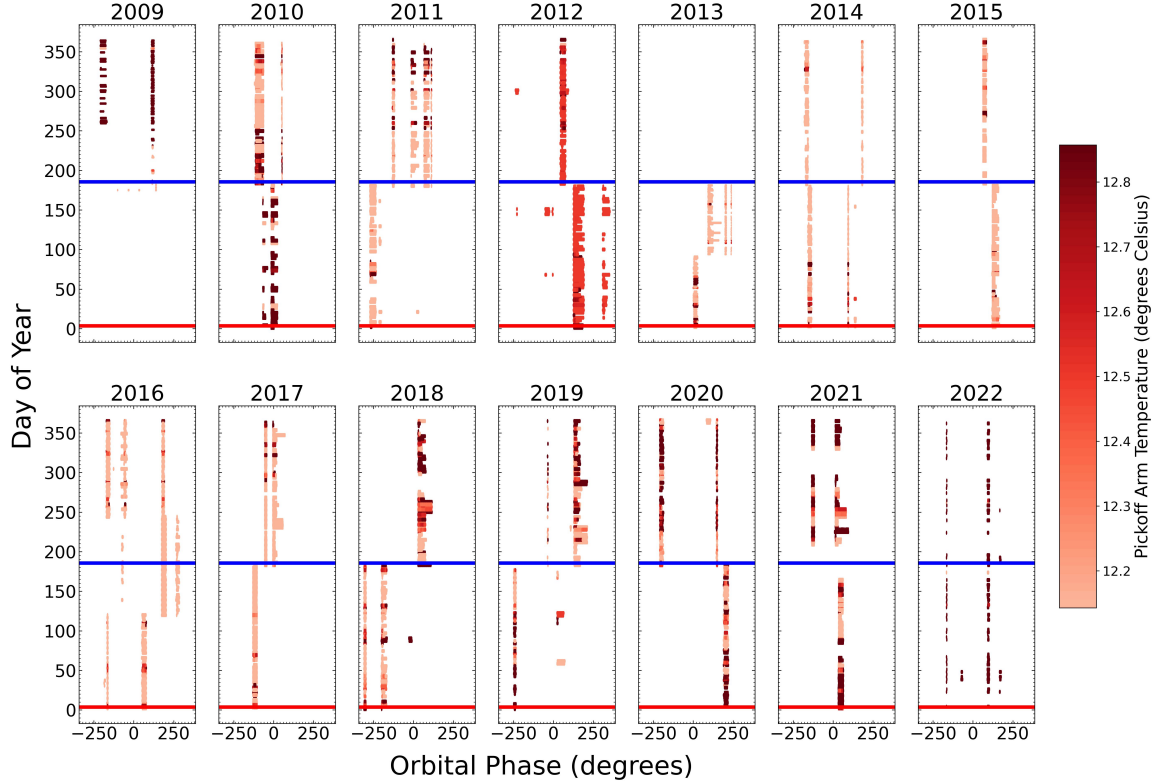


Figure 5 Pick-off arm temperature vs. day of the year and orbital phase (degrees), where the color represents T_{POM} (degrees Celsius). The horizontal red lines indicate where the Earth is closest to the Sun and the horizontal blue lines indicate where Earth is furthest from the Sun.

for these changes is the solar cycle. However, we do not believe that this is the cause of these variations, because the relevant solar maximum occurred in 2013 and solar minimum in 2019, when *HST* temperatures were rising (Biesecker and Upton, 2019).

One item to note is that while this trend is observed when focusing on T_{POM} , when some other sensors are studied their variations are much less significant. Figure 8 depicts the temperatures of three other components of WFC3 for the same observations as our pick-off arm data. Similar to the pick-off arm, the maximum and minimum temperatures of the cold plate and infrared focal plane array are within 1 degree Kelvin, and the temperatures of these sensors fluctuate less than T_{POM} , indicating that they are more stable. The optical bench near the condenser saddle do exhibit a wider range of temperatures, with the maximum temperature being approximately 14°C warmer than the minimum temperature. However, there is no strong correlation between time of year and the temperature of this component. These findings suggests that the temperature of *HST* is more stable near the detector than in more distant

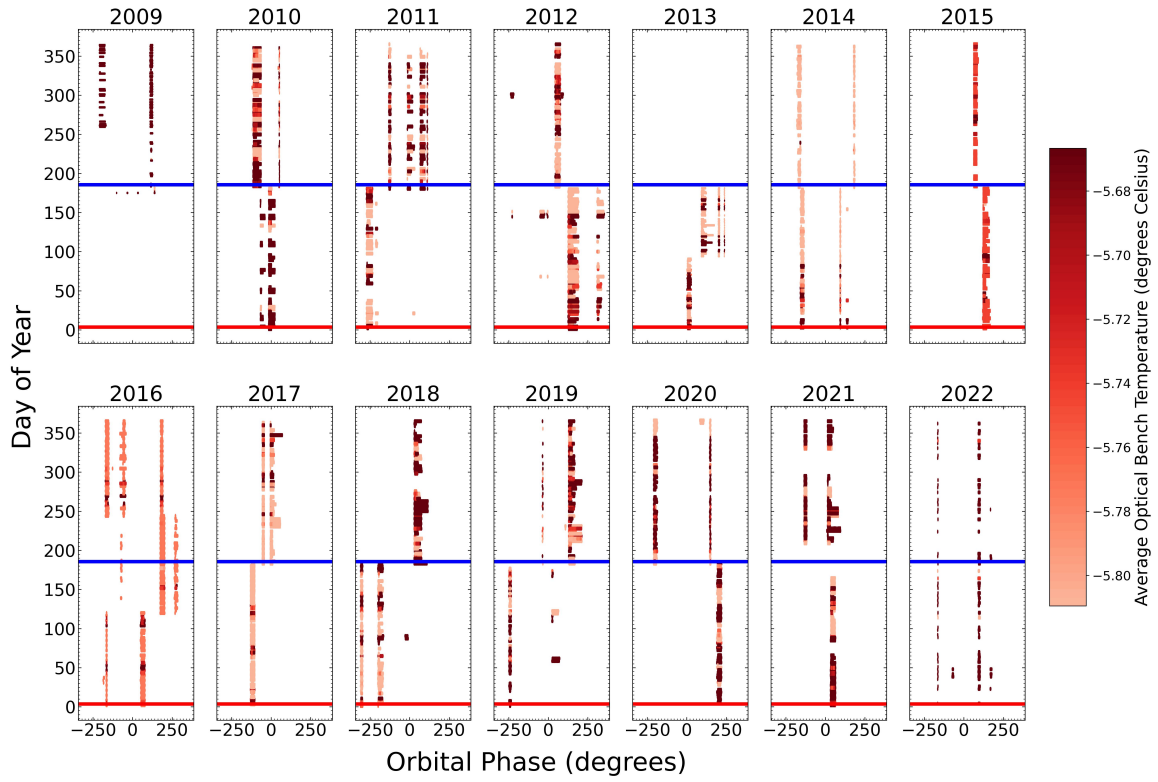


Figure 6 Optical bench temperature vs. day of the year and orbital phase (degrees), where the color representing average optical bench temperature (degrees Celsius).

parts of the telescope like the pick-off arm. This is logical, given that the majority of the instrument's cooling is focused around the detector.

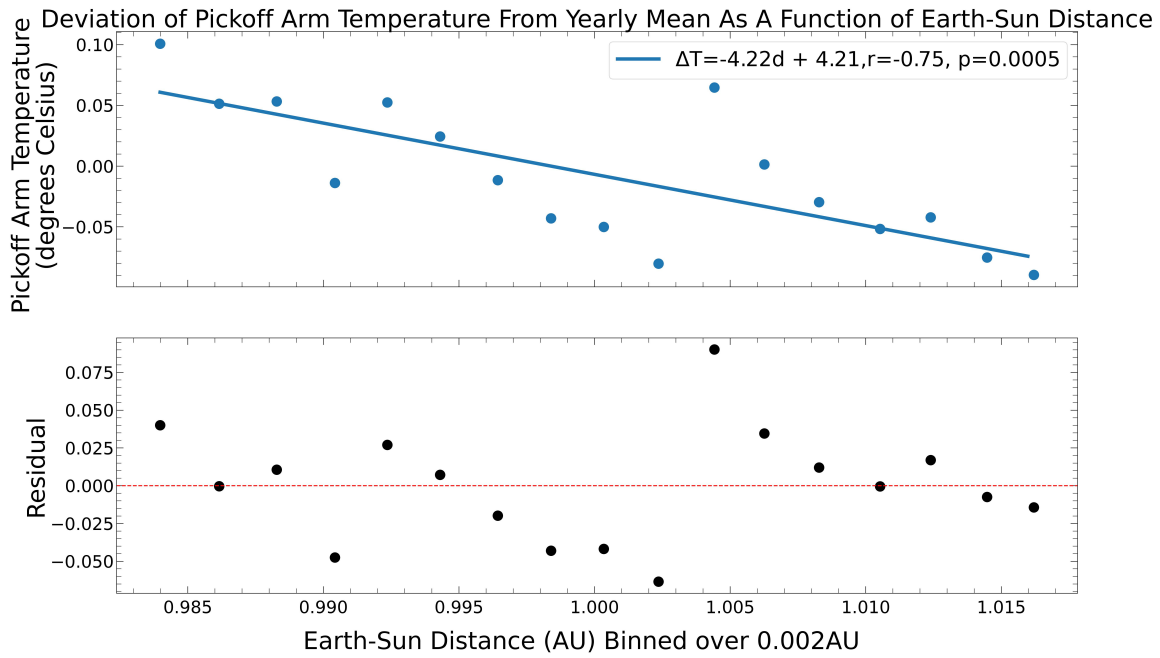


Figure 7 Model of the deviation in T_{POM} from the average yearly temperature as a function of the Earth-Sun distance. Error bars are calculated as the standard deviation of the residual.

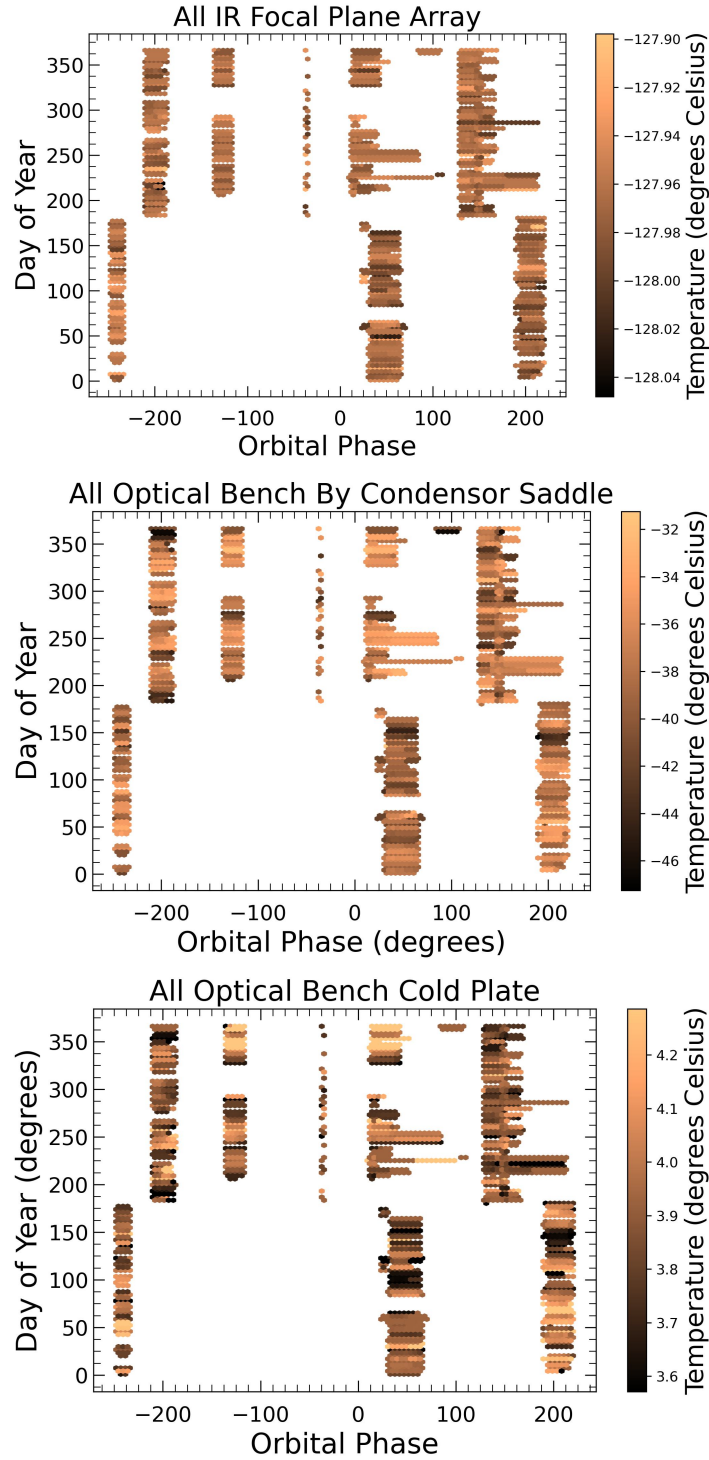


Figure 8 Temperatures of other WFC3 hardware components. Top: Temperature change of the IR focal plane array using data from 2009 through 2022. Middle: Temperature change of the optical bench condenser saddle using data from 2009 through 2022. Bottom: Temperature change of the optical bench cold plate using data from 2009 through 2022.

DISCUSSION

In Figure 9, we present our updated sky-surface brightness (sky-SB) measurements and compare them to the measurements presented in Bernstein *et al.* (2002), Matsuura *et al.* (2017), and O’Brien *et al.* (2023), as well as the Aldering (2001) zodiacal light model and the Kelsall *et al.* (1998) zodiacal light prediction. To obtain these measurements, we first calculate the thermal dark signal produced by the minimum and maximum T_{POM} and M1 temperature (see Table 2). Using this, we apply our correction to the sky-SB measurements published in O’Brien *et al.* (2023) in the F098M, F105W, F110W, F125W, F140W, and F160W filters. We use their pre-thermal dark correction sky-SB measurements for all images, where there are zero flags and where ecliptic latitude is between either 50 and 90° or −50 and −90°, to keep our measurements consistent with those in O’Brien *et al.* (2023) and to remove images with significant contaminated light. Next, we subtract our thermal dark measurements to obtain our updated sky-SB estimates. In general, we find somewhat lower sky-SB measurements in the F098M, F105W, F110W, F125W and F160W filters than in O’Brien *et al.* (2023), but a slightly higher sky-SB measurement in F140W. In addition, the differences in sky-SB measurements between the minimum and maximum and M1 temperatures are too small to be visible in Figure 9, indicating that temperature variations in *HST* have a minimal impact on our measurements (see Table 3). In Figure 10, we present our diffuse light limits alongside measurements taken from a wide variety of sources. Here, we observe limits on diffuse light generally lower than those produced in previous studies.

Table 2 Thermal dark corrections (in e-/pix/s) for all of the WFC3/IR filters included in this study.

Filter	T_{POM}	Thermal Dark		M1 Thermal Dark		Primary & Secondary	
	Min	Max	Min	Max	Min	Max	
F098M	0.00454	0.00454	0.00454	0.00454	0.00443	0.00444	
F105W	0.00455	0.00455	0.00455	0.00455	0.00444	0.00445	
F110W	0.00480	0.00480	0.00482	0.00482	0.00468	0.00483	
F125W	0.00479	0.00480	0.00482	0.00482	0.00467	0.00483	
F140W	0.0213	0.0216	0.0223	0.0223	0.0199	0.0277	
F160W	0.0807	0.0819	0.0843	0.0845	0.0739	0.1066	

Table 3 The diffuse light measurements of Carleton *et al.* (2022), O’Brien *et al.* (2023), and this work based on the combined primary, secondary, and T_{POM} temperatures. Conversions between MJy/sr to $\text{nW m}^{-2} \text{sr}^{-1}$ were done using the multipliers in Carleton *et al.* (2022).

Source	Units	F125W	F140W	F160W
Carleton <i>et al.</i> (2022)	MJy/sr	0.012	0.025	0.048
	$\text{nW m}^{-2} \text{sr}^{-1}$	29	40	29
O’Brien <i>et al.</i> (2023)	MJy/sr	0.009	0.015	0.013
	$\text{nW m}^{-2} \text{sr}^{-1}$	22	32	25
This work, upper limit	MJy/sr	0.009	0.015	0.013
	$\text{nW m}^{-2} \text{sr}^{-1}$	21	32	25
This work, max thermal dark possible	MJy/sr	0.009	0.013	0.005
	$\text{nW m}^{-2} \text{sr}^{-1}$	21	29	10

To confirm our thermal dark corrections, we take the difference between the sky-SB measurements provided in O’Brien *et al.* (2023) and the Carleton *et al.* (2022) zodiacal light predictions for the F125W, F140W, and F160W filters. Then, we apply our updated thermal dark corrections for the primary, secondary, and pick-off mirrors to each point and take the difference between that and the Carleton *et al.* (2022) zodiacal light predictions (Figure 11).

Several possible explanations exist to explain the data we are observing. First, the variations in temperature within a single year are most likely the result of the Earth’s orbit around the Sun. The temperature of *HST* is at its highest in the year when Earth is closest to the Sun at the beginning and end of the year, and coolest in the middle of the year when the Earth is furthest from the Sun.

The cause of the changes in temperature from year to year are not presently fully understood. We investigated the solar cycle as a possible explanation for this change. However, the solar minimum occurred in 2019, which does not align with the results that we have observed. The increase in temperature from 2016 until the present may be a result of degradation of *HST*’s MLI on *HST*’s outer tube over time (Biesecker and Upton, 2019). Because the variations in temperature are less than one degree Celsius, we have shown that these fluctuations impact our measurements of diffuse light by less than 0.01 MJy/steradian.

The WFC3 broad-band spectra of asteroids and Kuiper Belt Objects (KBOs) is known to peak around $1.4 \mu\text{m}$ wavelength (see e.g., Fig. 8 of Fraser *et al.*, 2015), and

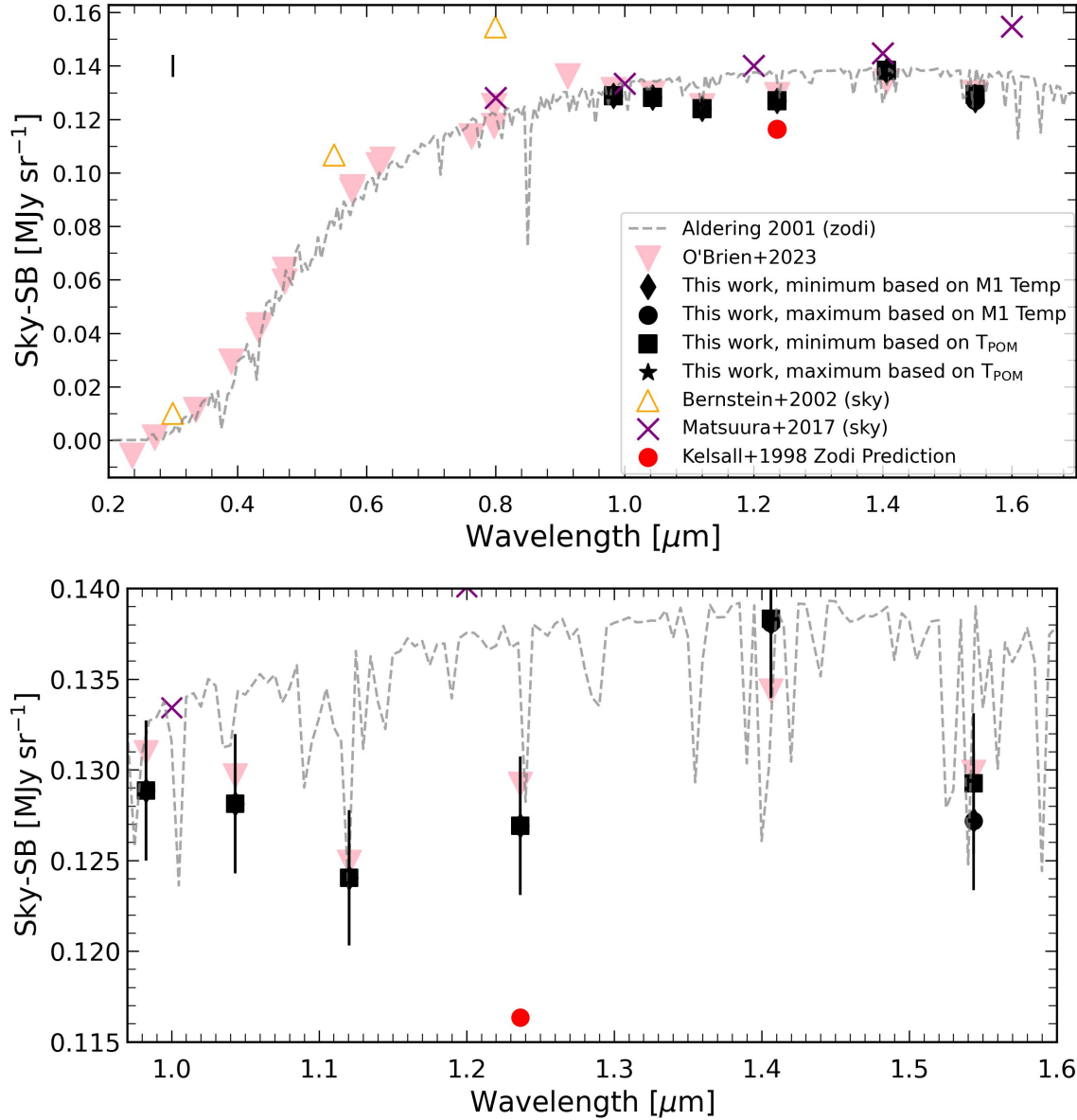


Figure 9 Top: Sky surface brightness measurements from this work for maximum and minimum (T_{POM}) and M1 temperature measurements, compared to those from Bernstein *et al.* (2002), Matsuura *et al.* (2017), and O'Brien *et al.* (2023), and the zodiacal light models from Aldering (2001) and Kelsall *et al.* (1998). The vertical line in the top left of the plot represents the average size of the error bars for these measurements. Errors are assumed to be approximately 3%, per Windhorst *et al.* (2022). Bottom: A zoomed-in version of the top plot to highlight the differences between instrument components and maximums and minimums.

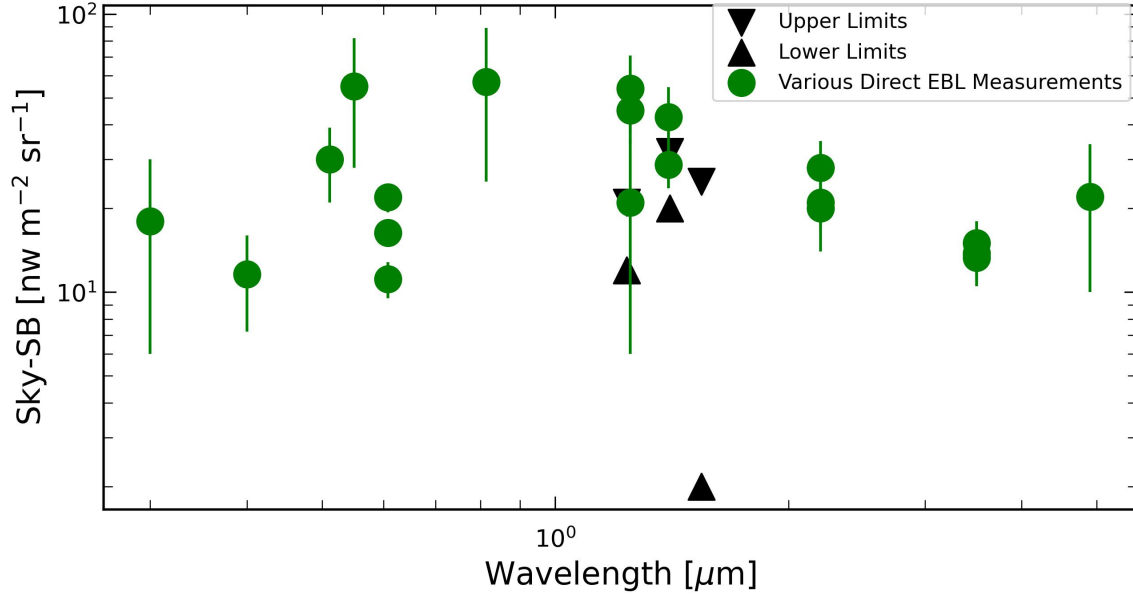


Figure 10 The diffuse light measurements found in Dube *et al.* (1979), Dwek and Arendt (1999), Cambr sy *et al.* (2001), Bernstein *et al.* (2002), Arendt and Dwek (2003) Levenson *et al.* (2007), Mattila *et al.* (2017), Matsuura *et al.* (2017), Sano *et al.* (2020), Lauer *et al.* (2022), Symons *et al.* (2023), and Postman *et al.* (2024) compared with our upper and lower limits on diffuse light. Our limits are lower than the previous measurements of diffuse light.

so a dim dilute cloud of Zodiacal icy dust could slightly perturb and enhance the Zodiacal spectrum at 1–1.6 μm wavelength. Modeling the exact modified shape and amplitude of the Zodiacal spectrum at 1–1.6 μm wavelength is beyond the scope of the current paper, but is being pursued through a modified Kelsall *et al.* (1998) model by R. O’Brien *et al.* (in preparation).

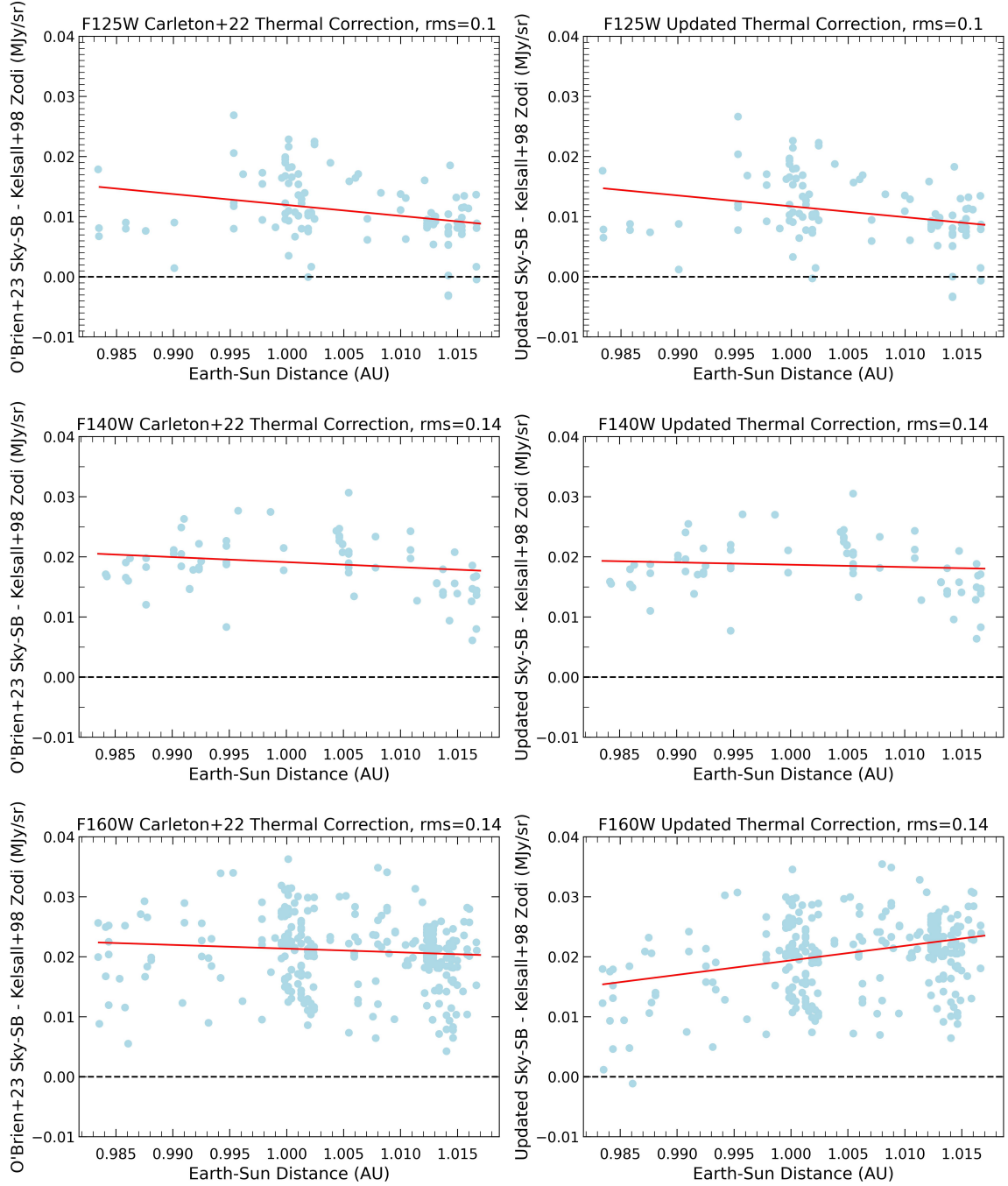


Figure 11 Top left: Residual between O'Brien *et al.* (2023) sky surface brightness measurements and Kelsall *et al.* (1998) zodiacal light model (extrapolated to redder wavelengths following Carleton *et al.* (2022)) in the F125W filter using the thermal dark correction from Carleton *et al.* (2022). The red line is the line of best fit for these data. Top right: Residual between O'Brien *et al.* (2023) sky surface brightness measurements and Kelsall *et al.* (1998) zodiacal light model in the F125W filter using the empirical thermal dark correction this work. The red line is the line of best fit for these data. Middle left: Same as top left, but using the F140W filter. Middle right: Same as top right, but using the F140W filter. Bottom left: Same as top left, but using the F160W filter. Bottom right: Same as top right, but using the F160W filter.

CONCLUSION AND FUTURE OUTLOOK

In this paper, we discuss the impact of changes in HST thermal emission on diffuse light measurements. We find that while WFC3/IR remains at a relatively constant temperature with changing orbital phase and time since occultation, (T_{POM}) changes by $\lesssim 1$ K with Earth-Sun distance and year of observation. We also find empirical evidence of variation in the thermal background beyond this range, which is consistent with $\pm \sim 3.5$ K variation of the primary and secondary mirror expected over the course of a year. Our direct and empirical temperature estimates agree that the average thermal background is consistent with the default ($\Delta T = 0$ K) value, as opposed to the $\Delta T = -1.15$ K value adopted in Carleton *et al.* (2022) and O’Brien *et al.* (2023). We model these changes and examine their impact on the diffuse light measurements provided in Carleton *et al.* (2022) and O’Brien *et al.* (2023).

Based on the updated pick-off arm temperatures identified in Sec. 2, as well as the empirical estimates of the primary and secondary mirror temperatures, we estimate that the median thermal background levels range from 0.0047 e-/s/pix in F125W, 0.0217 e-/s/pix in F140W, and 0.082 e-/s/pix in F160W. Based on these updates to the thermal background level, we update diffuse light limits of O’Brien *et al.* (2023) to 21 nW m⁻² sr⁻¹, 32 nW m⁻² sr⁻¹, and 25 nW m⁻² sr⁻¹ in the F125W, F140W, and F160W filters, respectively. These limits are lower those provided in Carleton *et al.* (2022) and O’Brien *et al.* (2023).

After reducing the uncertainty on the thermal dark emission from HST, we find that a significant diffuse sky signal in SKYSURF data. As a conservative lower limit on the level of diffuse emission, we combine the remaining uncertainty on the thermal emission (taking the max TD possible values from Table 3) with the $\sim 1\%$ uncertainty on the WFC3IR zero-point (Bajaj *et al.*, 2020). This results in lower limits (3σ) of 12 nW m⁻² sr⁻¹, 20 nW m⁻² sr⁻¹, and 2 nW m⁻² sr⁻¹ in F125W, F140W, and F160W respectively. In the context of recent New Horizons results from (Postman *et al.*, 2024), which find that the level of diffuse light is less than 8 nW m⁻² sr⁻¹ (3σ), the signal observed in the SKYSURF data may be due to a very dim Zodiacal light source, possibly from icy dust in the inner Solar System (e.g., Fraser *et al.*, 2015). Notably, icy objects, and by extension cometary icy dust, appear to show a peak in their IR SEDs around 1.4 μ m, like the diffuse signal we observe.

BIBLIOGRAPHY

- Aldering, G., “Snap sky background at the north ecliptic pole”, LBNL report **LBNL-51157**, 1, 1–12 (2001).
- Arendt, R. G. and E. Dwek, “An Empirical Decomposition of Near-Infrared Emission into Galactic and Extragalactic Components”, **585**, 1, 305–318 (2003).
- Bajaj, V., A. Calamida and J. Mack, “Updated WFC3/IR Photometric Calibration”, Instrument Science Report WFC3 2020-10, 19 pages (2020).
- Bernstein, R. A., W. L. Freedman and B. F. Madore, “The First Detections of the Extragalactic Background Light at 3000, 5500, and 8000 Å. I. Results”, **571**, 1, 56–84 (2002).
- Biesecker, D. A. and L. Upton, “Solar Cycle 25 Consensus Prediction Update”, in “AGU Fall Meeting Abstracts”, vol. 2019, pp. SH13B-03 (2019).
- Cambrésy, L., W. T. Reach, C. A. Beichman and T. H. Jarrett, “The Cosmic Infrared Background at 1.25 and 2.2 Microns Using DIRBE and 2MASS: A Contribution Not Due to Galaxies?”, **555**, 2, 563–571 (2001).
- Carleton, T., R. A. Windhorst, R. O’Brien, S. H. Cohen, D. Carter, R. Jansen, S. Tompkins, R. G. Arendt, S. Caddy, N. Grogin, S. J. Kenyon, A. Koekemoer, J. MacKenty, S. Casertano, L. J. M. Davies, S. P. Driver, E. Dwek, A. Kashlinsky, N. Miles, N. Pirzkal, A. Robotham, R. Ryan, H. Abate, H. Andras-Letanovszky, J. Berkheimer, Z. Goisman, D. Henningsen, D. Kramer, C. Rogers and A. Swirbul, “SKYSURF: Constraints on Zodiacal Light and Extragalactic Background Light through Panchromatic HST All-sky Surface-brightness Measurements: II. First Limits on Diffuse Light at 1.25, 1.4, and 1.6 μm ”, **164**, 5, 170 (2022).
- Cleveland, P. E., M. T. Buchko, R. A. Stavely and B. T. Pham, “Thermal vacuum test performance of the hubble space telescope (hst) wide field camera 3 (wfc3) variable conductance heat pipe assembly”, (2003).
- Conselice, C. J., A. Wilkinson, K. Duncan and A. Mortlock, “The Evolution of Galaxy Number Density at $z < 8$ and Its Implications”, **830**, 2, 83 (2016).
- Cooray, A., “Extragalactic background light measurements and applications”, Royal Society Open Science **3**, 3, 150555 (2016).
- Cooray, A., J. J. Bock, B. Keatin, A. E. Lange and T. Matsumoto, “First Star Signature in Infrared Background Anisotropies”, **606**, 2, 611–624 (2004).

- Dressel, L. and M. Marinelli, “WFC3 Instrument Handbook for Cycle 31 v. 15.0”, in “WFC3 Instrument Handbook for Cycle 31 v. 15.0”, vol. 15, p. 15 (2023).
- Driver, S. P., S. K. Andrews, L. J. Davies, A. S. G. Robotham, A. H. Wright, R. A. Windhorst, S. Cohen, K. Emig, R. A. Jansen and L. Dunne, “Measurements of Extragalactic Background Light from the Far UV to the Far IR from Deep Ground- and Space-based Galaxy Counts”, **827**, 2, 108 (2016).
- Dube, R. R., W. C. Wickes and D. T. Wilkinson, “Upper limit on the extragalactic background light.”, **232**, 333–340 (1979).
- Dwek, E. and R. G. Arendt, “A tentative detection of the cosmic infrared background at $3.5 \mu\text{m}$ from COBE/DIRBE observations”, in “After the Dark Ages: When Galaxies were Young (the Universe at $2 < Z < 5$)”, edited by S. Holt and E. Smith, vol. 470 of *American Institute of Physics Conference Series*, pp. 354–358 (AIP, 1999).
- Fraser, W. C., M. E. Brown and F. Glass, “The Hubble Wide Field Camera 3 Test of Surfaces in the Outer Solar System: Spectral Variation on Kuiper Belt Objects”, **804**, 1, 31 (2015).
- Kashlinsky, A., R. Arendt, J. P. Gardner, J. C. Mather and S. H. Moseley, “Detecting Population III Stars through Observations of Near-Infrared Cosmic Infrared Background Anisotropies”, **608**, 1, 1–9 (2004).
- Kelsall, T., J. L. Weiland, B. A. Franz, W. T. Reach, R. G. Arendt, E. Dwek, H. T. Freudenreich, M. G. Hauser, S. H. Moseley, N. P. Odegard, R. F. Silverberg and E. L. Wright, “The COBE Diffuse Infrared Background Experiment Search for the Cosmic Infrared Background. II. Model of the Interplanetary Dust Cloud”, **508**, 1, 44–73 (1998).
- Kneiske, T. M. and H. Dole, “A lower-limit flux for the extragalactic background light”, **515**, A19 (2010).
- Koushan, S., S. P. Driver, S. Bellstedt, L. J. Davies, A. S. G. Robotham, C. d. P. Lagos, A. Hashemizadeh, D. Obreschkow, J. E. Thorne, M. Bremer, B. W. Holwerda, A. M. Hopkins, M. J. Jarvis, M. Siudek and R. A. Windhorst, “GAMA/DEVILS: constraining the cosmic star formation history from improved measurements of the $0.3\text{--}2.2 \mu\text{m}$ extragalactic background light”, **503**, 2, 2033–2052 (2021).
- Lauer, T. R., M. Postman, J. R. Spencer, H. A. Weaver, S. A. Stern, G. R. Gladstone, R. P. Binzel, D. T. Britt, M. W. Buie, B. J. Buratti, A. F. Cheng, W. M. Grundy, M. Horányi, J. J. Kavelaars, I. R. Linscott, C. M. Lisse, W. B. McKinnon, R. L. McNutt, J. M. Moore, J. I. Núñez, C. B. Olkin, J. W. Parker, S. B. Porter, D. C. Reuter, S. J. Robbins, P. M. Schenk, M. R. Showalter, K. N. Singer, A. J. Verbiscer

- and L. A. Young, “Anomalous Flux in the Cosmic Optical Background Detected with New Horizons Observations”, **927**, 1, L8 (2022).
- Lauer, T. R., M. Postman, H. A. Weaver, J. R. Spencer, S. A. Stern, M. W. Buie, D. D. Durda, C. M. Lisse, A. R. Poppe, R. P. Binzel, D. T. Britt, B. J. Buratti, A. F. Cheng, W. M. Grundy, M. Horányi, J. J. Kavelaars, I. R. Linscott, W. B. McKinnon, J. M. Moore, J. I. Núñez, C. B. Olkin, J. W. Parker, S. B. Porter, D. C. Reuter, S. J. Robbins, P. Schenk, M. R. Showalter, K. N. Singer, A. J. Verbiscer and L. A. Young, “New Horizons Observations of the Cosmic Optical Background”, **906**, 2, 77 (2021).
- Levenson, L. R., E. L. Wright and B. D. Johnson, “DIRBE Minus 2MASS: Confirming the CIRB in 40 New Regions at 2.2 and 3.5 μm ”, **666**, 1, 34–44 (2007).
- MacKenty, J. W., R. A. Kimble, R. W. O’Connell and J. A. Townsend, “On-orbit performance of HST Wide Field Camera 3”, in “Space Telescopes and Instrumentation 2010: Optical, Infrared, and Millimeter Wave”, edited by J. Oschmann, Jacobus M., M. C. Clampin and H. A. MacEwen, vol. 7731 of *Society of Photo-Optical Instrumentation Engineers (SPIE) Conference Series*, p. 77310Z (2010).
- Matsumoto, T., S. Matsuura, H. Murakami, M. Tanaka, M. Freund, M. Lim, M. Cohen, M. Kawada and M. Noda, “Infrared Telescope in Space Observations of the Near-Infrared Extragalactic Background Light”, **626**, 1, 31–43 (2005).
- Matsuura, S., T. Arai, J. J. Bock, A. Cooray, P. M. Korngut, M. G. Kim, H. M. Lee, D. H. Lee, L. R. Levenson, T. Matsumoto, Y. Onishi, M. Shirahata, K. Tsumura, T. Wada and M. Zemcov, “New Spectral Evidence of an Unaccounted Component of the Near-infrared Extragalactic Background Light from the CIBER”, **839**, 1, 7 (2017).
- Mattila, K., P. Väisänen, K. Lehtinen, G. von Appen-Schnur and C. Leinert, “Extragalactic background light: a measurement at 400 nm using dark cloud shadow - II. Spectroscopic separation of the dark cloud’s light, and results”, **470**, 2, 2152–2169 (2017).
- McVittie, G. C. and S. P. Wyatt, “The Background Radiation in a Milne Universe.”, **130**, 1 (1959).
- O’Brien, R., T. Carleton, R. A. Windhorst, R. A. Jansen, D. Carter, S. Tompkins, S. Caddy, S. H. Cohen, H. Abate, R. G. Arendt, J. Berkheimer, A. Calamida, S. Casertano, S. P. Driver, C. Gelb, Z. Goisman, N. Grogin, D. Henningsen, I. Huckabee, S. J. Kenyon, A. M. Koekemoer, D. Kramer, J. Mackenty, A. Robotham and S. Sherman, “SKYSURF-4: Panchromatic Hubble Space Telescope All-Sky Surface-brightness Measurement Methods and Results”, **165**, 6, 237 (2023).

- Partridge, R. B. and P. J. E. Peebles, “Are Young Galaxies Visible?”, **147**, 868 (1967).
- Postman, M., T. R. Lauer, J. W. Parker, J. R. Spencer, H. A. Weaver, J. M. Shull, S. A. Stern, P. Brandt, S. J. Conard, G. R. Gladstone, C. M. Lisse, S. D. Porter, K. N. Singer and A. J. Verbiscer, “New Synoptic Observations of the Cosmic Optical Background with New Horizons”, arXiv e-prints p. arXiv:2407.06273 (2024).
- Sahu, K., “WFC3 Data Handbook v. 5”, in “WFC3 Data Handbook v. 5”, vol. 5, p. 5 (2021).
- Sano, K., S. Matsuura, K. Yomo and A. Takahashi, “The Isotropic Interplanetary Dust Cloud and Near-infrared Extragalactic Background Light Observed with COBE/DIRBE”, **901**, 2, 112 (2020).
- Santos, M. R., V. Bromm and M. Kamionkowski, “The contribution of the first stars to the cosmic infrared background”, **336**, 4, 1082–1092 (2002).
- Sosey, M. L. and A. Sivaramakrishnan, “The thermal background of HST as measured by HST-NICMOS”, in “Optical, Infrared, and Millimeter Space Telescopes”, edited by J. C. Mather, vol. 5487, pp. 299 – 307, International Society for Optics and Photonics (SPIE, 2004), URL <https://doi.org/10.1117/12.550484>.
- Sunnquist, B., S. Baggett and K. S. Long, “A Predictive WFC3/IR Dark Current Model”, Instrument Science Report WFC3 2017-24, 31 pages (2017).
- Symons, T., M. Zemcov, A. Cooray, C. Lisse and A. R. Poppe, “A Measurement of the Cosmic Optical Background and Diffuse Galactic Light Scaling from the $R < 50$ au New Horizons-LORRI Data”, **945**, 1, 45 (2023).
- Virtanen, P., R. Gommers, T. E. Oliphant, M. Haberland, T. Reddy, D. Cournapeau, E. Burovski, P. Peterson, W. Weckesser, J. Bright, S. J. van der Walt, M. Brett, J. Wilson, K. J. Millman, N. Mayorov, A. R. J. Nelson, E. Jones, R. Kern, E. Larson, C. J. Carey, Í. Polat, Y. Feng, E. W. Moore, J. VanderPlas, D. Laxalde, J. Perktold, R. Cimrman, I. Henriksen, E. A. Quintero, C. R. Harris, A. M. Archibald, A. H. Ribeiro, F. Pedregosa, P. van Mulbregt and SciPy 1.0 Contributors, “SciPy 1.0: Fundamental Algorithms for Scientific Computing in Python”, *Nature Methods* **17**, 261–272 (2020).
- Windhorst, R. A., T. Carleton, R. O’Brien, S. H. Cohen, D. Carter, R. Jansen, S. Tompkins, R. G. Arendt, S. Caddy, N. Grogin, A. Koekemoer, J. MacKenty, S. Casertano, L. J. M. Davies, S. P. Driver, E. Dwek, A. Kashlinsky, S. J. Kenyon, N. Miles, N. Pirzkal, A. Robotham, R. Ryan, H. Abate, H. Andras-Letanovszky, J. Berkheimer, J. Chambers, C. Gelb, Z. Goisman, D. Henningsen, I. Huckabee, D. Kramer, T. Patel, R. Pawlikar, E. Pringle, C. Rogers, S. Sherman, A. Swirbul

and K. Webber, “SKYSURF: Constraints on Zodiacal Light and Extragalactic Background Light through Panchromatic HST All-sky Surface-brightness Measurements. I. Survey Overview and Methods”, **164**, 4, 141 (2022).

Windhorst, R. A., S. H. Cohen, R. A. Jansen, J. Summers, S. Tompkins, C. J. Conselice, S. P. Driver, H. Yan, D. Coe, B. Frye, N. Grogin, A. Koekemoer, M. A. Marshall, R. O’Brien, N. Pirzkal, A. Robotham, R. E. Ryan, C. N. A. Willmer, T. Carleton, J. M. Diego, W. C. Keel, P. Porto, C. Redshaw, S. Scheller, S. M. Wilkins, S. P. Willner, A. Zitrin, N. J. Adams, D. Austin, R. G. Arendt, J. F. Beacom, R. A. Bhatawdekar, L. D. Bradley, T. Broadhurst, C. Cheng, F. Civano, L. Dai, H. Dole, J. C. J. D’Silva, K. J. Duncan, G. G. Fazio, G. Ferrami, L. Ferreira, S. L. Finkelstein, L. J. Furtak, H. B. Gim, A. Griffiths, H. B. Hammel, K. C. Harrington, N. P. Hathi, B. W. Holwerda, R. Honor, J.-S. Huang, M. Hyun, M. Im, B. A. Joshi, P. S. Kamieneski, P. Kelly, R. L. Larson, J. Li, J. Lim, Z. Ma, P. Maksym, G. Manzoni, A. K. Meena, S. N. Milam, M. Nonino, M. Pascale, A. Petric, J. D. R. Pierel, M. d. C. Polletta, H. J. A. Röttgering, M. J. Rutkowski, I. Smail, A. N. Straughn, L.-G. Strolger, A. Swirbul, J. A. A. Trussler, L. Wang, B. Welch, J. S. B. Wyithe, M. Yun, E. Zackrisson, J. Zhang and X. Zhao, “JWST PEARLS. Prime Extragalactic Areas for Reionization and Lensing Science: Project Overview and First Results”, **165**, 1, 13 (2023).